Niemelä, Janne-Petteri; Karttunen, Antti; Karppinen, Maarit

Inorganic-organic superlattice thin films for thermoelectrics

Published in:
Journal of Materials Chemistry C

DOI:
10.1039/C5TC01643F

Published: 01/01/2015

Document Version
Peer-reviewed accepted author manuscript, also known as Final accepted manuscript or Post-print

Journal of Materials Chemistry C

REVIEW-TYPE ARTICLE

Inorganic-organic superlattice thin films for thermoelectrics

J.-P. Niemelä[a], A. J. Karttunen[a] and M. Karppinen[a,*]

Received 00th January 20xx,
Accepted 00th January 20xx

DOI: 10.1039/x0xx00000x

www.rsc.org/

Nanoscale layer-engineering is an attractive tool to tailor the performance of thermoelectric materials as it potentially allows us to suppress thermal conductivity without significantly hindering the electrical transport properties. By combining the state-of-the-art thin-film fabrication technique for inorganics, *i.e.* atomic layer deposition (ALD), with its emerging counterpart for the organics, *i.e.* molecular layer deposition (MLD), it is possible to fabricate in a single reactor oxide-organic thin-film superlattices in which periodically introduced single/few-molecule organic layers alternate with thicker thermoelectric oxide layers. In such fundamentally new types of superlattice materials the oxide-organic interfaces with notable property mismatch are anticipated to hinder the phonon transport and/or bring about charge confinement effects thereby enhancing the material´s thermoelectric figure-of-merit. The experimental data so far gathered for the (Zn,Al)O:HQ and (Ti,Nb)O_2:HQ systems (HQ stands for hydroquinone) show significantly suppressed thermal conductivities. Here in this topical review we summarize the experimental and computational works carried out on these superlattice materials and discuss the future potential of the ALD/MLD-fabricated inorganic-organic superlattice and nanolaminate thin-film structures in thermoelectrics.

1. Introduction

Striving for a truly energy efficient society demands that increasing efforts will be made to harvest the huge quantities of heat wasted by both industrial processes and domestic appliances. The key technology to answer to the call is the thermoelectric (TE) power generation that enables direct conversion of heat to electricity with all-solid-state TE devices.[1] On the other hand, the continuous downscaling of microelectronic devices calls for more efficient cooling systems for portable devices – an issue which could be solved by utilizing localized thin-film TE coolers.[2]

In the core of making better TE devices is to enhance the performance of the existing heavily-doped n- and p-type semiconducting TE materials, that is, to increase their thermoelectric figure-of-merit zT ($\equiv S^2\sigma T/\kappa$, where S is the Seebeck coefficient, σ electronic conductivity and κ thermal conductivity; $S^2\sigma$ is the power factor (PF)). Typical zT values for commercial bismuth telluride alloys are around unity at room temperature, but can be enhanced in nanostructures[2] (see Table 1). Increasing the zT value is a challenging task, as the three material parameters, S, σ and κ, are intimately bound by conflicting dependencies on the carrier density (electron or hole). However, as heat is not only carried by electrons but also by phonons, κ can be partially decoupled from S and σ, and is hence typically expressed as $\kappa = \kappa_l + \kappa_e$, where κ_l stands for the phonon and κ_e for the electronic contribution. Such a decoupling provides us with a means of designing routes to suppress κ_l without a notable cost in S and σ – an effect that can be achieved by employing phonon-blocking/electron-transmitting material structures.

Superlattices are thin-film materials where alternating layers of dissimilar materials enable the blocking of phonon transport by internal interface-scattering, and provided that the periodicity of the superlattice is properly set, the electronic properties can be kept essentially unaffected or even enhanced. The enhancement in electronic properties may originate from *e.g.* quantum-confinement effects, thermionic effects in heterostructures, carrier-pocket engineering and energy filtering;[2,3] illustrative examples of inorganic superlattices are *e.g.*, PbTe/$Pb_{1-x}Eu_xTe$[4] and Si/Ge[5]. Currently, due to the highly promising results gained through phonon engineering, the primary focus in the efforts to increase the z value is more and more shifted to finding the most effective ways to suppress the κ_l values. For superlattices with densely spaced layers the superlattice period is the key parameter to control the phonon transport, as scattering by internal interfaces apparently dominates over the scattering by the bulk of the constituent materials:[6] for incoherent phonons κ_l is efficiently suppressed by decreasing the period, until potentially, phonon coherence may yield an upturn for periods similar to (and smaller than) the phonon mean free path.[7,8]

Experimental studies on inorganic superlattices such as GaAs/AlAs and Si/Ge have shown that not only does the control over the superlattice period provide us with a prominent tool to realize order-of-magnitude drops in cross-plane[9] thermal conductivity values but significant suppressions can be achieved also in the in-plane[10] direction. The discovery of considerably reduced thermal conductivity values in superlattices led to a number of theoretical studies in the field,

[a] Department of Chemistry, Aalto University, FI-00076 Espoo, Finland
* email: maarit.karppinen@aalto.fi

which sought to provide explanation for the reduction in both in-plane[11] and cross-plane[12,13] thermal conductivity in superlattices. A recent review by Kazan and Masri on the contribution of surfaces and interfaces to the crystal thermal conductivity discusses the theoretical approaches in this field in more detail.[14] In general, the κ values reported, *e.g.*, for W/Al_2O_3 nanolaminates[15] (~0.6 $Wm^{-1}K^{-1}$ at 300 K) and layered WSe_2 crystals[16] (~0.05 $Wm^{-1}K^{-1}$ at 300 K) underline the power of layered structures for achieving ultra-low thermal conductivity values (*via* careful balancing of order and disorder) comparable to those of amorphous or even porous materials.[17]

Besides the simple size effects, in multilayers of dissimilar materials thermal conductivity can be further controlled *via* careful tailoring of the internal interfaces. Inorganic and organic materials show notable misfit in the phonon density of state spectra – a desired dissimilarity – that may lead to a very low thermal boundary conductance over the inorganic-organic interface.[18] Control over the strength of the chemical bond between the inorganic and organic layers offers us an additional parameter for tuning the thermal boundary conductance.[19] Also, one could benefit from phonon filtering effects brought about by a destructive interference within the organic layer for properly chosen polymer-chain lengths.[20] Moreover, as another option to exploit carbon-based intermittent layers (besides the molecular organic layers) within an inorganic matrix van-der-Waals bonded graphene interlayers have been demonstrated to have a lowering effect on the thermal boundary conductance.[21] The recent report on layered TiS_2 with intercalated organic molecules showing a zT value of 0.28 at 373 K further encourages to strive research on inorganic-organic materials for thermoelectrics (see Table 1).[22]

An elegant way to fabricate inorganic-organic multilayers and superlattices in thin-film form is to employ the state-of-the-art thin-film technique for the inorganics, *i.e*. atomic layer deposition (ALD) in combination with the more recently developed molecular layer deposition (MLD) technique for organics.[23-25] Both techniques rely on self-saturating gas-to-surface reactions that guarantee the thin-film fabrication with atomic/molecular monolayer precision; for recent comprehensive reviews see Refs. 26 and 27. A common feature of both ALD and MLD is the perfect conformality of the resultant thin-film coating over a variety of imaginative nanostructures – a key strength that makes the two techniques a driving force for future nanotechnologies.[28] Moreover, the organic layers in the hybrid films can be transformed into graphitic carbon layers *via* a post-deposition annealing to form yet a new class of nanocomposite thin-film materials with enhanced performance, *e.g.* in terms of thermal stability.[29,30] In particular, the precise control over the layer spacing and the drastic vibrational dissimilarity expected between the inorganic ALD layers and the organic MLD layers make the ALD/MLD hybrid thin films and superlattices attractive low thermal conductivity and thermoelectric materials; so far the experimental proof-of-the-concept data are for the two oxide materials, ZnO and TiO_2, combined with single organic hydroquinone-based layers or graphitic-type carbon layers.[31-33] The novel inorganic-organic hybrid materials have also been recently studied with state-of-the-art computational methods, providing detailed atomic-level information on their structure-property correlations.[34,35] In this topical review we summarize the experimental and theoretical work carried out in the field that is strongly emerging, yet in its infancy.

Table 1 *Illustrative thermoelectric transport properties for a Bi_2Te_3/Sb_2Te_3 superlattice thin film[2] with record-high performance and for a promising hybrid TiS_2/organic (organic = $[(hexylammonium)_x(H_2O)_y(dimethylsulphoxide)_z]$) superlattice[22] (at 300 K). The abbreviation ip stand for in-plane and cp for cross-plane direction. The numbers marked with ~ were approximated from figures or calculated from the reported parameters.*

Material	ρ (mΩcm)	S (μV/K)	κ ($Wm^{-1}K^{-1}$)	PF ($\mu Vcm^{-1}K^{-2}$)	zT
Bi_2Te_3/Sb_2Te_3 (cp)	0.85	~200	~0.6	~50	2.4
TiS_2/organic (ip)	1.3	-78	0.69	4.5	0.2

2. Fabrication of oxide-organic superlattice thin films with the ALD/MLD technique

The ALD technique is a sophisticated thin-film technique that has become the method of choice in *e.g*. semiconductor industry for fabricating homogeneous pinhole-free oxide and sulphide thin films on large-area and/or nanostructured substrates in a highly reproducible and conformal manner.[35,36,26,28] The technique is based on sequential introduction of gaseous precursors into the ALD reactor and their self-saturating gas-surface reactions. To fabricate thin films of binary oxide materials such as ZnO or TiO_2, vapours of a suitable metal precursor (*e.g*. $Zn(CH_2CH_3)_2$ or $TiCl_4$) and an oxygen source (*e.g.* water) are alternately pulsed into the reaction chamber in a sequence of four steps constituting together a so-called ALD cycle, as illustrated in Fig. 1. The thin-film material with the desired thickness is then grown by simply repeating the basic ALD cycle a given number of times (m), thus ideally controlling the film thickness with a precision of an atomic monolayer. In practice even in a well-behaving ALD process the film growth rate may be lower than the ideal monolayer *per* cycle, due to *e.g*. steric hindrance caused by bulky ligands in the precursors.

Self-limited routes to deposit thin-film materials can also be designed for purely organic precursors; then the technique is called molecular layer deposition,[27] and examples of the organic polymeric materials grown by MLD include various polyimide and polyamide films.[37-40] Most interestingly, bringing together the versatile sets of the conventional ALD precursors for metals and the organic MLD precursors, such as different organic alcohols,[41,42] carboxylic acids[43,44] or amines,[45,46] enables the deposition of inorganic-organic hybrid thin films.[41,27] It is remarkable that besides simple homogeneous hybrid thin-film materials, the combined ALD/MLD technique allows the fabrication of inorganic-organic nanolaminates[46-48] and – particularly to the present work – superlattices[23-25] with atomic/molecular monolayer precision.

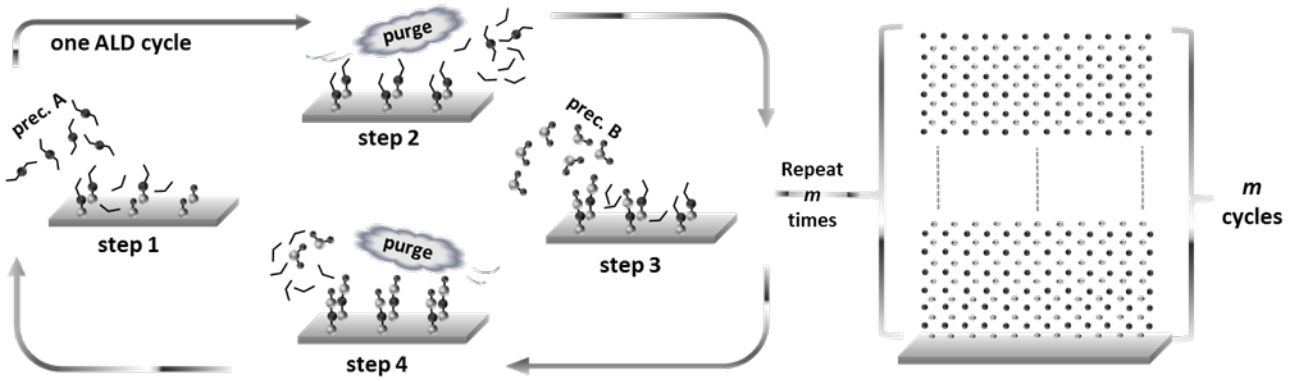

Figure 1. Schematic illustration of an ALD cycle employed to grow (ideally) a monolayer of a binary oxide (*e.g*. ZnO). One ALD cycle consists of four individual steps: (1) pulsing of the metal precursor (*e.g.* diethylzinc) and its chemisorption on the surface, (2) purging of the excess precursor and byproduct molecules with inert gas (*e.g*. N_2), (3) pulsing of the oxygen source (*e.g.* water) and its reaction with the metal precursor on the surface, and (4) purging of the excess precursor and byproduct molecules. A thin film of the target compound of the desired thickness is then grown by repeating the four-step ALD cycle a specified number of times, *m*.

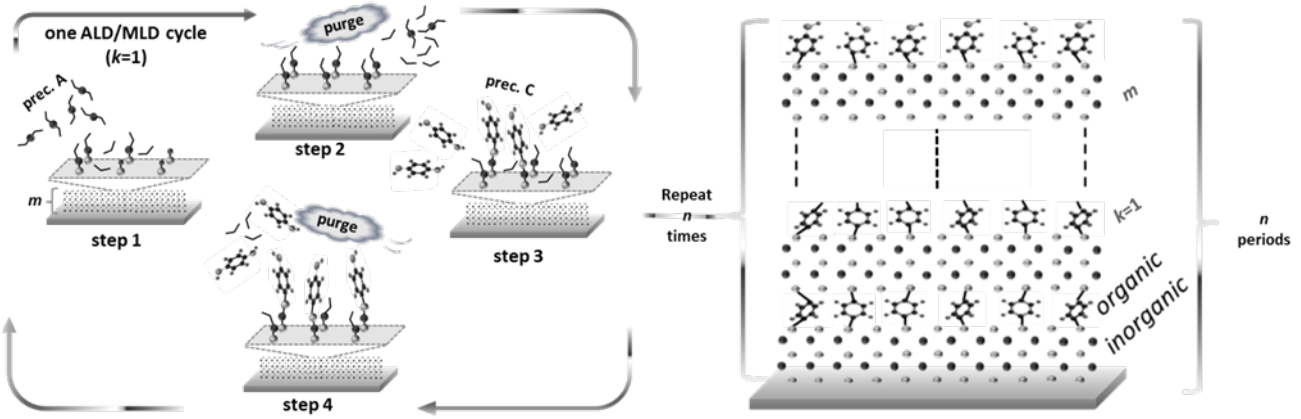

Figure 2. A schematic illustration of an ALD/MLD cycle to grow a monolayer of the metal-organic molecules between thicker oxide layers: (1) pulsing of the metal precursor (*e.g.* diethylzinc) and its chemisorption on the surface, (2) purging of the excess precursor and byproduct molecules with inert gas (*e.g*. N_2), (3) pulsing of the organic precursor (*e.g.* hydroquinone) and its reaction with the metal precursor on the surface, and (4) purging of the excess organic precursor and byproduct molecules. A superlattice film of the type $[(ZnO)_m(Zn\text{-}O\text{-}C_6H_4\text{-}O\text{-})_{k=1}]_n$ of a desired thickness is grown by repeating the set of *m* ALD cycles and *k* (=1) ALD/MLD cycles *n* times, where *n* is the number of superlattice periods.

Fabrication of an inorganic-organic superlattice *via* an ALD/MLD route and a representation of the resultant superlattice structure are illustrated schematically in Fig. 2. To grow *e.g*. ZnO-based superlattice thin films of the $[(ZnO)_m(Zn\text{-}O\text{-}C_6H_4\text{-}O\text{-})_k]_n$ type we start by depositing a thicker (*m* ALD cycles) layer of the inorganic material (*e.g.* ZnO) in a manner described in Fig. 1, and then continue by depositing one (in case of *k* = 1) ALD/MLD cycle of the hybrid material on top of the inorganic layer, as shown in Fig. 2. By repeating such a layer combination of *m* ALD and *k* = 1 ALD/MLD cycles *n* times yields an inorganic-organic superlattice thin film with *n* periods (written as $[(ZnO)_m(Zn\text{-}O\text{-}C_6H_4\text{-}O\text{-})_{k=1}]_n$) with mono-molecular organic layers confined periodically within the inorganic matrix. Ideally, the single molecule-thick organic layers deposited by one ALD/MLD cycle consist of the backbone of the organic precursor, *e.g*. benzene ring in the case of the hydroquinone precursor, bonded *via* strong (covalent) chemical bonds to the oxide layers – a fact that stems inherently from the nature of the growth mechanism of the ALD and MLD processes. It should hence be emphasized that the growth mechanism requires the organic precursor molecule to contain two functional groups (*i.e*. bifunctional) in minimum. Also note that the number of subsequent ALD/MLD cycles is not limited to one (*k*=1); this has just been a practical choice in our first experiments for the sake of simplicity.

In practice, the ALD/MLD thin films are typically fabricated in ALD reactors evacuated to base pressures of the order of 10 mbar, while the deposition temperatures tend to be above 100 ^oC; generally an inert gas such as N_2 is used to carry the volatile precursors into the reactor chamber from precursor containers located outside the reactor chamber. Many precursors (such as DEZ, $TiCl_4$ and H_2O) are volatile enough at room temperature but for some reactants heating is applied (≥120 ^oC for HQ) to increase their vapour pressure. The pulse times required for reaching the saturation of the surface reactions may vary with the reactor design; roughly, however, the metal-precursor and water pulse lengths of around a second or even fractions of it suffice, while for the organic precursors

longer pulse lengths of the order of 10 s may be needed. In order to avoid overlapping of the consecutive precursor exposures and any gas-phase reactions between them, the duration of the purge periods typically exceeds those of the corresponding precursor exposures. As the films grow by thickness increments of few Ångströms *per* deposition cycle it takes from few tens of minutes to several hours to fabricate thin films with thicknesses in the range of tens of nanometers to few hundreds of nanometers.

3. Experimental and computational verification of the ALD/MLD superlattice structures

3.1. Experimental characterization

The terminology related to multilayer thin-film structures, *i.e.* superlattice *versus* nanolaminate, used in the literature varies and the distinction between them is not always clear-cut. We have not required single crystallinity and/or lattice match for the term superlattice; we rather like to reserve the term superlattice for the inorganic-organic multilayer structures where the number of the individual molecular layers in the organic part between thicker inorganic layer-blocks is limited to one or very few. The key techniques that have been used for the structural characterization of the ALD/MLD-fabricated superlattice thin films include X-ray reflection (XRR), Fourier-transform infrared spectroscopy (FTIR) and grazing-incidence X-ray diffraction (GIXRD).

At small incidence angles X-rays reflected from the film-air and the film-substrate interfaces interfere; this is detected as periodic oscillation of the reflected intensity, frequently referred to as Kiessieg fringes, whose periodicity carries information on the thickness of a thin film (small peaks in the XRR pattern, Fig. 3(a)). A similar interference effect is observed for X-rays reflected from the internal interfaces of a superlattice such that the XRR pattern shows a combination of reflections that depend on the number of the repeated superlattice periods, *n* (higher peaks, Fig. 3(a)). Ideally, *n*-2 small fringes are found between the successive large fringes – a detail that for the ALD/MLD superlattices enables the verification of the fact that the organic molecules indeed are periodically confined between the inorganic layers. Moreover, the angular separation of the superlattice peaks have shown a match with the expected superlattice period, as a further proof of the formation of the targeted inorganic-organic superlattice structures with a precise interface control. Based on XRR, ZnO-based superlattice thin films have been successfully grown not only with hydroquinone (HQ) molecules but also with 4-aminophenol (AP) and 4,4'-oxydianiline (ODA) molecules as organic precursors.[49]

As expected for the ALD/MLD processes using organic alcohols as a precursor, it has been shown that the organic molecules confined between the inorganic layers do bond *via* oxygen atoms to the metal atoms of the inorganic layers, a broad C-O stretching peak around 1196 cm^{-1} in the FTIR spectra being the finger print. The most pronounced feature in the FTIR spectra (see Fig. 3(b)) is the very clear absorption peak at around 1486 cm^{-1} corresponding to the C=C stretching in the aromatic rings from the HQ precursor, which together with a weak aromatic ring signal at 1589 cm^{-1} implies that the aromatic rings have been delivered to the superlattice structure intact. Crystallinity of the superlattices has been found to depend on the inorganic compound, as has been evidenced by the GIXRD technique. For the $[(TiO_2)_m(Ti\text{-}O\text{-}C_6H_4\text{-}O\text{-})_{k=1}]_n$ films the introduction of the organic molecules affects the crystallinity of the TiO_2 layers even at the composition of *m*:*k* = 400:1 (superlattice period of ~16 nm), whereas for the $[(ZnO)_m(Zn\text{-}O\text{-}C_6H_4\text{-}O\text{-})_{k=1}]_n$ films the crystallinity of the ZnO layers remains essentially unchanged at least down to superlattice periods of around 3 nm. Strong crystallization tendency for ZnO is expected, as ALD-fabricated ZnO films can crystallize even at room temperature.[50-51] Indeed, Liu *et al.* reported ZnO layers to crystallize even for the *k*:*m* ratio 1:1 for hybrids fabricated 150 at °C.[31] So far the effect of the deposition temperature on the crystallinity of the films has not been studied in great detail (210 °C for the TiO_2-based, and 220 °C for the ZnO-based films), but surely by adjusting the deposition temperature crystallinity of the inorganic layers could be improved, particularly in the case of the TiO_2-based films. In the case of ZnO, the deposition temperature also affects the preferred orientation of the films; therefore, adjusting the deposition temperature could also allow for tuning any orientation-dependent properties of the films (see section 4.1. below for details).[50-51] Furthermore, the control over the film orientation could improve comparability between the experimental results and the theoretical models, as in the latter a certain orientation must typically be assumed. Moreover, post-deposition annealing treatments could offer another route to enhanced crystallinity of the superlattices.

Interestingly, when high-enough annealing temperatures are applied under a reductive atmosphere molecular organic layers may transform into sub-nanometer-thick graphitic carbon layers thus yielding yet a new class of composite inorganic-C superlattice structures – here, this was achieved applying a heat treatment at 600 °C for 6 h under a flowing H_2/Ar (5/95 %) gas mixture. For these inorganic-C superlattices the Raman spectra show prominent peaks for sp^2 carbon at 1338 cm^{-1} and 1602 cm^{-1}, typically labeled as disordered D and graphitic G, respectively, and a modulated bump between 2400 and 3000 cm^{-1} consisting of second-order peaks of D peak overtone G' and the combination mode D + G.[52] The D peak is a breathing mode of A_{1g} symmetry with its intensity strictly connected to the presence of six-fold aromatic rings; the mode is forbidden in perfect graphite and only becomes active in the presence of disorder. The G peak stems from bond-stretching motion of pairs of carbon atoms both in rings and chains, and has E_{2g} symmetry. Fitting the spectral range of the D and G peaks using a Lorentzian for the D peak and a Breit-Wigner-Fano distribution for the G peak (inset of Fig. 3(d)) and analyzing the data against the model of Ferrari and Robertson[52] has indicated that the carbon present in the annealed inorganic-C films is probably best described as a mixture of nanocrystalline graphite and amorphous carbon,

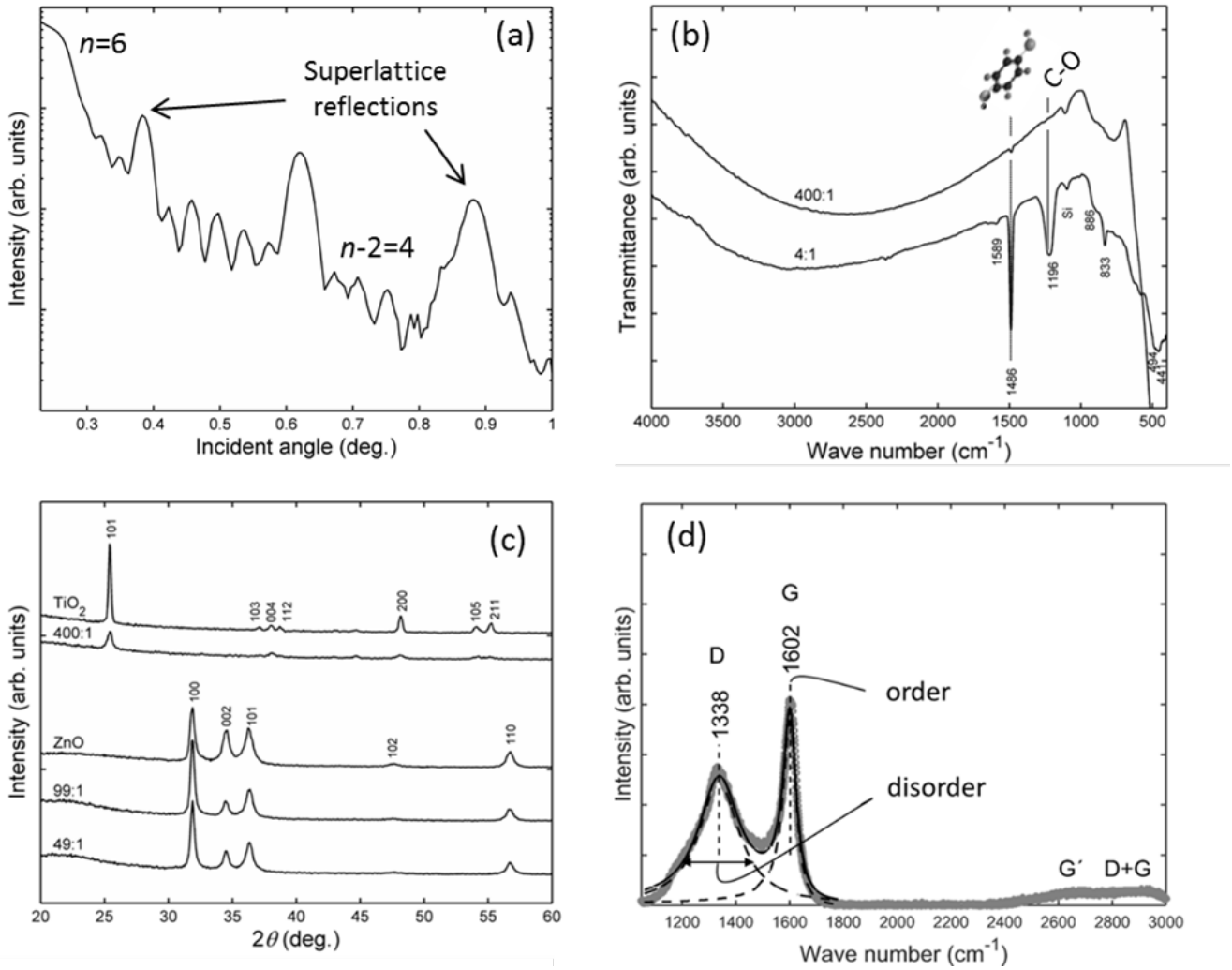

Figure 3. Typical structural characteristics for ALD/MLD-fabricated superlattice thin films. (a) XRR pattern with superlattice reflections for a $[(TiO_2)_m(Ti\text{-}O\text{-}C_6H_4\text{-}O\text{-})_{k=1}]_n$ film with n = 6. (b) FTIR spectra for $[(TiO_2)_m(Ti\text{-}O\text{-}C_6H_4\text{-}O\text{-})_{k=1}]_n$ superlattices with composition of m:k = 400:1 and 4:1. (c) GIXRD patterns for purely inorganic TiO_2 and ZnO films, and for a $[(TiO_2)_m(Ti\text{-}O\text{-}C_6H_4\text{-}O\text{-})_{k=1}]_n$ film with m:k = 400:1 and for $[(ZnO)_m(Zn\text{-}O\text{-}C_6H_4\text{-}O\text{-})_{k=1}]_n$ films with m:k = 99:1 and 49:1; the TiO_2 peaks are indexed to the tetragonal anatase phase, and the ZnO peaks to the hexagonal wurtzite structure. (d) Raman spectra for $[(Ti_{0.75}Nb_{0.25}O_2)_mC_{k=1}]_n$ film with the k:m ratio of 1:200 obtained via annealing in Ar/H_2 gas at 600 °C. Also shown is the fitting of the D and G peaks using a Lorentzian for the D peak and a Breit-Wigner-Fano distribution for the G peak.

as crystallinity is seen in the high G position value and amorphous character in the broadening of the D peak.

3.1. Computational characterization

Since the synthesis of inorganic-organic hybrid materials inevitably encompasses more variables to be optimized in comparison to the synthesis of simple inorganic materials, the experimental investigations on hybrid materials can greatly benefit from integration with state-of-the-art materials-modelling methods. Computational first-principles investigations that do not include any empirical, material-dependent parametrization enable the systematic atomic-level investigation of structure-property correlations, facilitating the interpretation, rationalization, and improvement of material properties.[53] Furthermore, modern atomistic materials modelling methods could provide us with powerful tools for high-throughput screening of potential functional materials.[54]

While the hybrid nature of the inorganic-organic materials adds a new level of complexity to the atomic-level description of the structures, *ab initio*/first-principles density functional theory (DFT) methods are in principle directly applicable to this new class of materials without the need for re-parametrization of the methods.[55] However, the true applicability of the *ab initio* methods also needs to be tested carefully because not all *ab initio* approaches can properly describe both the inorganic and organic parts and the interfaces between them. The challenges in the *ab initio* modelling of inorganic-organic hybrid materials were recently discussed by Draxl *et al.*[56] Focusing on solid-state hybrid materials, they addressed the question to what extent the hybrid materials can be quantitatively described with *ab initio* methods and where

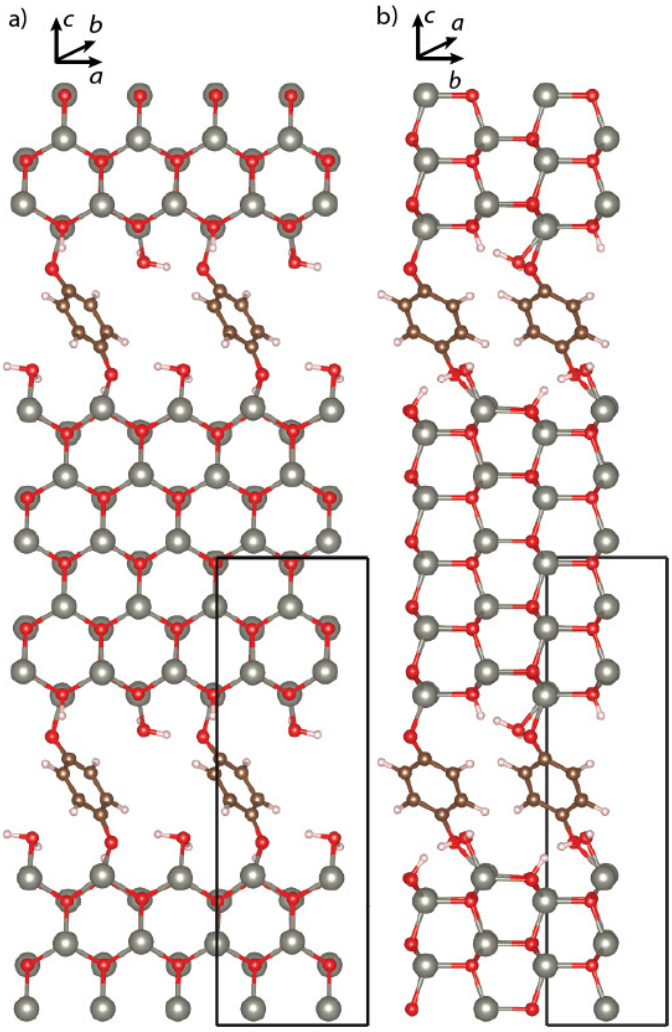

Figure 4. Optimized structure of ZnO:HQ superlattice with ZnO block thickness of 1.2 nm (DFT-PBE0/TZVP level of theory, unit cell denoted with black lines). The superlattice axes are not the same as for the hexagonal bulk ZnO. a) Viewed along the *b* axis. b) Viewed along the *a* axis.

even a qualitative description cannot be reached. The prediction of structural properties, electronic bands, optical excitation spectra, and charge transport in various organic-inorganic interfaces were discussed based on previous literature on computational studies with DFT and many-body perturbation methods.

State-of-the-art DFT methods were recently applied in several computational investigations on the structural and electronic properties of functional hybrid inorganic-organic materials and interfaces. Noori and Giustino investigated the energy-level alignment at the ZnO/poly(3-hexylthiophene) (P3HT) photovoltaic interface.[57] Large-scale, explicit atomistic models were used to describe the ZnO/P3HT interface and the energy-level alignment in a prospective hybrid inorganic-organic solar cell. Xu *et al.* investigated the adsorption of tetrafluoro-tetracyanoquinodimethane (F4TCNQ) on ZnO(000-1) surfaces.[58] Using explicit atomistic models for the ZnO/F4TCNQ interface, they studied how the adsorption energy and electron transfer depend on the ZnO doping and found a strong dependence. Finally, Hofmann *et al.* investigated the adsorption of pyridine on ZnO(10-10) using thermal desorption and photoelectron spectroscopy combined with computational DFT studies.[59] They showed that the adsorption of pyridine substantially reduces the work function of ZnO. Pyridine was found to adsorb upright, with all pyridine molecules aligned parallel to each other. In a closed monolayer, the pyridine molecules were bonded to every second surface Zn atom. Based on simple alignment considerations, they suggested that even larger work function modifications should be achievable using molecules with negative electron affinity. Importantly, such molecules could significantly reduce the electron injection barriers at ZnO-organic heterostructures.

We very recently derived the first atomic-level models of the hybrid ZnO:HQ materials, enabling detailed studies on their electronic, thermal and thermoelectric properties.[33] Explicit structural models for the ZnO:HQ superlattices with *a*-axis orientation for the ZnO were optimized using state-of-the-art hybrid density functional methods (DFT-PBE0/TZVP level of theory). The thickness of the ZnO block in the inorganic-organic superlattices varied from 1.2 to 11 nm, enabling comparisons with our experimental data. The smallest ZnO:HQ superlattice studied is illustrated in Fig. 4. We systematically investigated several different surface coverage models and bonding schemes for the ZnO:HQ interface. In the final model, 50% of the surface Zn sites are bonded to HQ molecule, while the other 50% of the Zn sites are saturated by water molecules. The 50% surface coverage is also in line with the recent experimental-theoretical study on pyridine adsorption on the ZnO(10-10) surface.[59] 100% coverage of the Zn surface sites by HQ molecules does not appear to be reasonable due to the high HQ–HQ repulsion arising from such a configuration.

Comparison between the predicted and experimental IR spectra for ZnO:HQ superlattices showed good agreement, enabling full assignment of the observed spectral features.[33,60] In the experimental spectrum, a very broad mode centred at about 3000 cm^{-1} is observed in the high frequency range (> 2000 cm^{-1}, similar to Fig. 3(b)). Detailed theoretical analysis of the vibrational modes showed that the high-frequency peaks arise from O–H stretching modes of the OH and H_2O surface species at the ZnO:HQ interface. Raman spectra for the ZnO:HQ superlattices were also predicted to enable comparisons with experimental spectra to be measured.

4. Thermoelectric properties of (Zn,Al)O:HQ and (Ti,Nb)O_2:HQ/C superlattice thin films

4.1. Electrical transport properties of (Zn,Al)O:HQ films

Zinc oxide is a wide band-gap (direct band gap of 3.37 eV at room temperature) semiconductor exhibiting intrinsically *n*-type conductivity due to unintentional defects forming during the material synthesis. Thin films of ZnO grown by one of the most common ALD processes, *i.e.* from diethyl zinc (DEZ) and H_2O precursors, are typically polycrystalline of the hexagonal wurtzite structure with a high degree of crystallinity even when using relatively low deposition temperatures.

Orientation of the grains depends on the deposition temperature: below 70 °C the grains show strong preference towards the *c*-axis orientation, then above 70 °C the *a*-axis orientation becomes gradually more prominent such that at around 160–200 °C the grains are predominantly oriented along the *a* axis, and finally above 220 °C the texture of the films switches again to the one dominated by the *c*-axis orientation.[51]

Partly because of the strong *n*-type character of undoped ZnO, it is difficult to induce *p*-type conductivity through acceptor dopants, but *n*-type doping is readily achieved with various trivalent cation dopants. For ALD-ZnO thin films, *n*-type doping is in a most straightforward manner realized by replacing a certain part of the DEZ/H_2O cycles with TMA/H_2O (TMA stands for trimethyl aluminum $Al(CH_3)_3$) cycles; for optimally Al-doped ZnO films grown by ALD resistivity values as low as 10^{-4} Ω cm have been obtained. The optimal Al-doping level to minimize the resistivity varies from study to study, being typically in the range of 2–5 %. At Al contents higher than this the resistivity increases as the solubility limit of Al into ZnO is exceeded.[51] The lightly Al-doped (Zn,Al)O films show also decent thermoelectric characteristics, *i.e*. decent negative Seebeck coefficient and low enough resistivity with maximum room-temperature power factor of 0.38 $\mu WK^{-2}cm^{-1}$ for 2 % Al-doping.[24] It should be kept in mind that in many ALD studies on Al-doped ZnO the actual Al content of the films has not been verified with elemental analysis techniques, so the reported doping levels typically represent the expected doping level calculated from the ratio of the TMA/H_2O and DEZ/H_2O ALD cycles rather than the actual Al content.

Then for creating the oxide-organic superlattices, the strength of the ALD/MLD approach stems from the deposition mechanism, *i.e*. the atomic/molecular level controllability acquired by the self-limiting surface reaction steps and the separation of the precursor supply steps. Thus, a single layer of an organic constituent can be created simply by inserting a single pulse of the organic precursor into the deposition program, while the length of the superlattice period is readily controlled by the number of ALD cycles between two MLD cycles and thereby the thickness of individual inorganic layers. The approach also allows for the simultaneous addition of metal dopant layers into the film structure, here by introducing single TMA/H_2O cycles between DEZ/H_2O cycles.

We have systematically exploited ALD-grown undoped and Al-doped ZnO films as the inorganic matrix for our oxide-organic superlattice thin films. The main advantages of the ALD-(Zn,Al)O system as a kind of model oxide matrix for these studies are that (*i*) the DEZ/H_2O and TMA/H_2O processes are both very well established and nearly ideal ALD processes, and (*ii*) the as-deposited films are very well crystallized already at relatively low deposition temperatures. Moreover, (*iii*) the relatively high lattice thermal conductivity of pristine ZnO leaves space for considerable gains in thermoelectric performance provided that our superlattice concept indeed works to reduce the lattice thermal conductivity. We fixed the deposition temperature at 220 °C for both the purely inorganic (Zn,Al)O films and the (Zn,Al)O:HQ superlattice films. From comprehensive characterizations by means of X-ray diffraction, X-ray reflection, X-ray fluorescence spectroscopy (XRF), optical reflectivity, Seebeck coefficient and resistivity measurements, the Al-doping was found to affect the carrier density of ZnO up to a nominal Al-dopant content of *ca*. 5 at.%; beyond that an inclusion of an amorphous phase presumably due to Al_2O_3 was observed and no further carrier doping of ZnO was realized. The thermoelectric power factor *PF* (≡ S^2/ρ, where ρ is resistivity) for purely inorganic (Zn,Al)O was maximized for the 2 at.% Al-doping level; doping levels up to this were thus selected a the compositions of the (Zn,Al)O matrix in our oxide-organic superlattice depositions. This is also the doping regime, where the DEZ/TMA/H_2O process deviates minimally from the ideal – that is, the nominal ALD cycle ratio (TMA/H_2O)/(TMA/H_2O + DEZ/H_2O) do not markedly differ from the measured atomic Al/(Al + Zn) ratio.[61,62] Our (Zn,Al)O:HQ superlattice thin films did not require any post-deposition anneal to *e.g*. improve the crystallinity or transport properties.[24]

As for the effect of the organic layers on the electronic transport properties of pure ZnO films, despite the relatively low concentration of the organic layers in the ZnO:HQ hybrid, the single-molecular organic layers have been found to cause a clear reduction in electrical conductivity in the undoped ZnO matrix (Fig. 5 (a)). However, this reduction can be more than compensated by the simultaneous Al-doping; this has been seen from both Seebeck coefficient (Fig. 5 (b)) and optical reflectivity measurements revealing essentially identical values for both $(Zn_{1-x}Al_x)O$ and $(Zn_{1-x}Al_x)O$:HQ films at the same Al content, *x*.[24] Most importantly, the changes seen in the resistivity and the Seebeck coefficient largely compensate each other leading the thermoelectric power factor to show more moderate changes (Fig. 5 (c)); notably, *e.g.* the 8 nm period ZnO:HQ superlattice shows equal in-plane power factor to that of the undoped ZnO film – simultaneous decrease in thermal conductivity would then lead to enhanced *zT*.

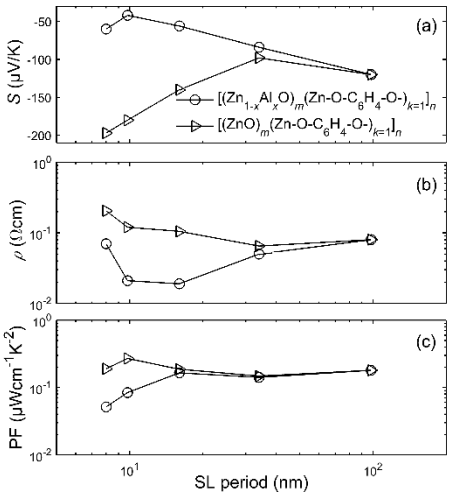

Figure 5. (a) Seebeck coefficient (*S*), (b) resistivity (ρ) and (c) the power factor S^2/ρ (PF) as a function of the superlattice period for $[(ZnO)_m(Zn\text{-}O\text{-}C_6H_4\text{-}O\text{-})_{k=1}]_n$ and $[(Zn_{1-x}Al_xO)_m(Zn\text{-}O\text{-}C_6H_4\text{-}O\text{-})_{k=1}]_n$ hybrid films. The Al content is $x = 1/(1+m)$, *i.e.*, the number of TMA /H_2O cycles equals to the number of DEZ/HQ cycles. Al content from left to right is $x = 0.02$, $x = 0.016$, $x = 0.01$, $x = 0.005$; the data points at ≈10^2 nm correspond to the undoped ZnO films.

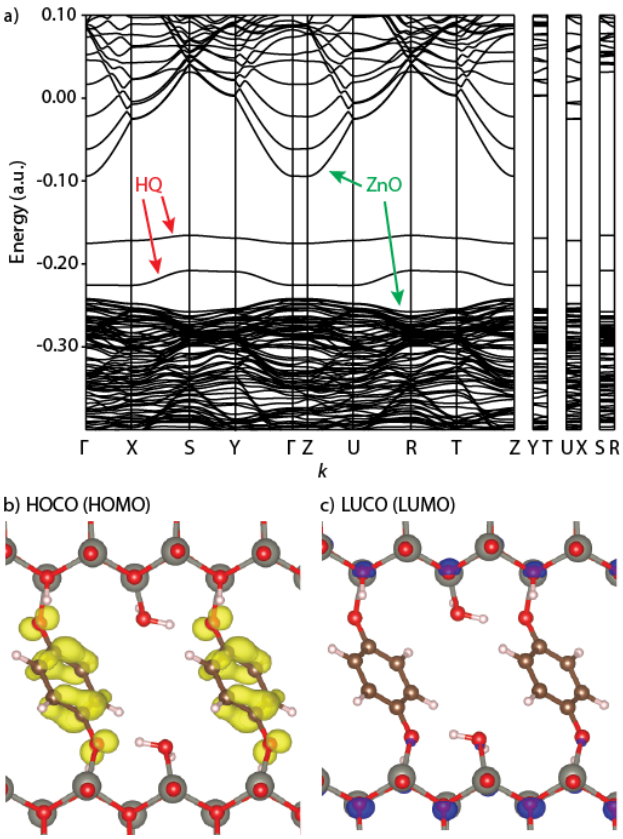

Figure 6. a) Band structure for ZnO:HQ superlattice with ZnO block thickness of 1.2 nm; b) Band-projected electron density for the highest energy valence band HOCO (density isovalue 0.01 a.u.); c) Band-projected electron density for the lowest energy conduction band LUCO (density isovalue 0.002 a.u.).

Computational studies on the ZnO:HQ superlattices have shown that the introduction of the HQ layers significantly affects the band structure of ZnO.[33] Molecular states arising from the HQ molecules are introduced into the ZnO band gap, changing the band gap from direct to indirect and decreasing its magnitude from 3.55 eV to 1.94 eV (Figure 6). The highest valence band in the ZnO:HQ superlattice is dominated by contributions from the organic HQ molecules while the conduction bands are ZnO-type, delocalized bands. A comparison between the band structure of bulk ZnO and the ZnO:HQ superlattice reveals that the group velocities of the conduction electrons are reduced in the ZnO:HQ superlattice, in particular for the *c*-direction, where the conduction bands become almost flat. This reduction in the electron group velocities is also in line with the experimentally observed reduction in the electrical conductivity due to the introduction of the organic layers. The electronic structure calculations also illustrate clearly how the band structure of the hybrid material could be tailored by simple and experimentally feasible modifications of the organic constituent. The first-principles studies can thus provide concrete examples on how the organic parts of the oxide-organic superlattice thermoelectric materials should be optimized to improve their electrical and thermoelectric properties.

4.2. Electrical transport properties of (Ti,Nb)O_2:HQ/C films

Titanium dioxide is an *n*-type semiconductor generally known for its photocalytic properties and as a dye-sensitized solar cell electrode material. However, the recent discovery of high electronic conductivity for Nb-doped anatase thin films has directed increasing attention towards the transport properties of TiO_2.[63]

In the absence of extrinsic dopants *n*-type conductivity in TiO_2 can be achieved by adjusting oxygen deficiency in the material structure, typically realized using strongly reductive fabrication conditions or by applying strongly reductive post-fabrication annealing treatments. For Nb-doped TiO_2, excess oxygen in the anatase structure is deleterious for electron conduction as interstitial oxygen can form *p*-type states that readily trap and compensate for the carrier electrons generated by the extrinsic dopants.[64] It is of note that, the tetragonal crystal structure of the material induces notable anisotropy to its transport properties:[65] the effective mass in the (*a*,*b*)-plane is by factor of 3-6 lower than in the *c*-axis direction; consequently, the minimum in-plane resistivity (~2×10^{-4} Ωcm at 300 K) can only be achieved in highly *c*-axis oriented thin films.

The previous reports on the thermoelectric properties of Nb-doped TiO_2 have indicated a room-temperature Seebeck coefficient around -60 μV/K, a reasonably high value that is accompanied by the very low resistivity to yield a considerably high power factor of S^2/ρ = 14 μW/(K²cm), close to that of bismuth telluride (37 μW/(K²cm)) peaking at 350 K.[66] Based on the thermal conductivity data by Tasaki *et al.*[67] (4-6 W m^{-1} K^{-1}), Jaćimović *et al.*[66] have estimated *zT* around 0.1-0.2 between 300 and 600 K for 6% Nb-doped anatase TiO_2 films.

A variety of ALD fabrication routes have been designed for deposition of TiO_2 thin films, among which by far the most common proceeds *via* sequential pulsing of the $TiCl_4$ and H_2O precursors; Ti deposits upon chemisorption of $TiCl_4$ and O after H_2O exposure, where the reaction between the chloride and hydroxyl groups yields HCl as a by-product for both the partial reactions. Crystallinity of the TiO_2 films fabricated using the $TiCl_4/H_2O$ process vary depending on the deposition temperature: between 100 and 165 °C the films grow amorphous, from 165 to 350 °C films with the anatase structure form, whereas above 350 °C mixed-phase films with anatase and increasing amount of rutile phase are obtained.[68]

Niobium-doped TiO_2 thin films can be fabricated by replacing a desired amount of the $TiCl_4/H_2O$ (or $Ti(OMe)_4/H_2O$[69]) ALD cycles by $Nb(OEt)_5/H_2O$ cycles; for these films deposited at temperatures around 210 °C incorporation of Nb dopant notably suppresses the crystallinity such that for the doping ratio Nb/(Nb+Ti) > 0.05, the films are practically amorphous.[70,71] Therefore, post-deposition annealing treatments at 500-600 °C have been applied to crystallize the films into the anatase structure; to obtain conductive films the annealing atmosphere has to be chosen strongly reductive to remove any excess oxygen from the anatase matrix. For the thus-far ALD-fabricated Nb:TiO_2 films electron mobility has been limited by grain boundary scattering in the low-doping

regime of Nb/(Nb+Ti) ≤ 0.15 and high-quality films free from inter-grain scattering have been obtained at the high-doping regime of Nb/(Nb+Ti) ≥ 0.20.[71] In the high-doping regime notably *c*-axis oriented very low-resistivity films ($\rho \approx 1$ mΩcm) with a performance similar to those of sputtered polycrystalline films are obtained; the drawback of the required heavy doping is that the Seebeck coefficient values corresponding to the minimum conductivity values drop to [-10,-20] μV/K,[70] thus for achieving all-optimal transport/thermoelectric properties, further research is required to inhibit grain-boundary scattering in the low doping regime. Altogether, Nb-doped TiO_2 is a material with promising thermoelectric properties, where further improvement to the thermoelectric performance can most likely be obtained by means of phonon engineering aiming at suppression of material's thermal conductivity.

Our approach to reduce materials' thermal conductivity has been to sandwich sub-nanometer-thick organic layers periodically between wider inorganic layers of thermoelectric oxides as phonon-scattering boundaries. In the case of TiO_2 this is realized by fabricating inorganic-organic $[(TiO_2)_m(Ti\text{-}O\text{-}C_6H_4\text{-}O\text{-})_{k=1}]_n$ superlattice thin films of total thickness of around 100 nm by depositing single (k=1) $TiCl_4$/HQ MLD cycles between wider (m>1) layers of TiO_2 deposited *via* the $TiCl_4/H_2O$ ALD route.[25] The composition of the films has been varied in a wide range 4:1 < m:k < 400:1 resulting in superlattice structures with the superlattice period ranging from 0.4 nm to 11 nm. Similar superlattices have also been fabricated with Nb:TiO_2 as the oxide matrix; here the Nb/(Nb+Ti) ratio was set to 0.25 in order to avoid the grain boundary scattering of the conduction electrons.

The introduction of organic layers notably affects the crystallinity of the $[(TiO_2)_m(Ti\text{-}O\text{-}C_6H_4\text{-}O\text{-})_{k=1}]_n$ films such that even for the films with a superlattice period of 11 nm crystallinity is suppressed and for even smaller periods the films become amorphous; all the Nb-doped superlattices have been found amorphous regardless of the superlattice period. When the insulating as-deposited films are annealed at 600 °C in Ar/H_2 the crystallinity is notably improved in a way that even the film with the period of 2 nm has been found relatively crystalline. Moreover, upon annealing the crystalline films become conductive. Most interestingly, we have noticed from Raman measurements that the annealing treatment converts the monomolecular HQ-based organic layers into amorphous/nanocrystalline graphitic interface layers (see Fig. 3 (d)) extraordinarily retaining the superlattice structure of the films as evidenced *via* XRR. Furthermore, we have observed that the film thickness decreases throughout the sample series upon annealing as an indication of increasing in-plane orientation of the aromatic rings.[29]

From four-point resistivity and Seebeck coefficient measurements carried out at 300 K in the in-plane direction for the annealed $[(Ti_{0.75}Nb_{0.25}O_2)_m(Ti\text{-}O\text{-}C_6H_4\text{-}O\text{-})_{k=1}]_n$ superlattices we have noticed that both of the properties remain relatively unchanged for superlattice periods larger than 5 nm. The resistivity values are around 1-2×10^{-3} Ωcm while the corresponding Seebeck coefficient values are around [-10,-12] μV/K – these values yield a rather constant power factor slightly below 0.1 μWK^{-2}cm^{-1}. For periods smaller than 5 nm the transport properties become notably suppressed, probably due to insufficient crystallinity or any barriers to electron transport created by the densely spaced organic layers. Altogether, the data have shown that sub-nanometer-thick graphitic layers can be sandwiched between Nb:TiO_2 layers by means of the ALD/MLD technique combined with a reductive annealing treatment, and that as long as the superlattice period remains larger than 5 nm the in-plane transport properties are not severely suppressed.

4.3 Thermal conduction properties

Above we described the electronic transport properties of the (Zn,Al)O:HQ and (Ti,Nb)O_2:HQ/C thin films separately – in this chapter we summarize the experimental thermal conductivity results for both the benchmark materials together, as in this respect their behaviour bear notable resemblance. The cross-plane thermal conductivity values have been measured with time-domain thermoreflectance (TDTR, University of Virginia) – a technique that uses a combination of laser pulses to reveal the thermal properties of the sample: first, pump pulses introduce a stimulus of thermal energy to a metal transducer (here Al) on the sample surface, and second, probe pulses detect the consequent change in reflectance determined by the thermal properties of the sample.[72-74]

In Fig. 7 we summarize the TDTR results obtained at 300 K for $[(Zn_{1-x}Al_xO_2)_m(Zn\text{-}O\text{-}C_6H_4\text{-}O\text{-})_{k=1}]_n$ and $[(Ti_{1-x}Nb_xO_2)_m(Ti\text{-}O\text{-}C_6H_4\text{-}O\text{-})_{k=1}]_n$ films as a function of the superlattice period; in the case of the TiO_2-based films the results are shown both for the as-deposited and the annealed superlattices, where in the latter case the HQ-based molecular monolayers have been transformed into graphitic interface layers. For both the ZnO-based and the TiO_2-based superlattices the introduction of organic layers (both molecular and graphitic) enable a very notable suppression in the thermal conductivity values in comparison to the respective purely inorganic films.[33,29] Thermal conductivities decrease with decreasing superlattice period as a sign of incoherent scattering of phonons from the inorganic-organic interfaces.[7,8] The lowest value obtained is below the amorphous limit of TiO_2, ultra-low 0.66±0.04 Wm^{-1}K^{-1} for the TiO_2:HQ superlattice with the period of around 0.5 nm; the corresponding values for the annealed TiO_2-based superlattices are almost equally low, the small difference most likely stemming from the improved crystallinity for the annealed films. An additional decrease in the thermal conductivity values can be achieved by introducing the ionic impurities, Al into ZnO and Nb into TiO_2; such is expected for increased scattering of phonons from the increased amount of point defects.

The temperature dependence of cross-plane thermal conductivity has been measured for ZnO-based superlattice films with periods of 7 nm and 13 nm at low temperatures between 70 and 300 K. For the smaller period superlattice the thermal conductivity remain below corresponding values for the larger period superlattice at all the measured

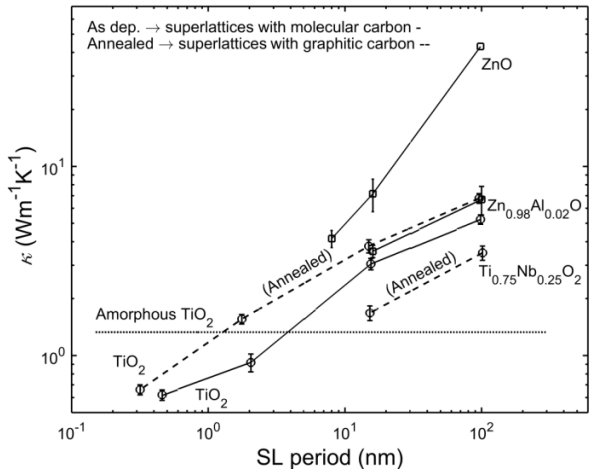

Figure 7. Thermal conductivity for the (Zn,Al)O:HQ and (Ti,Nb)O_2:HQ/C thin films as a function of the superlattice (SL) period; for TiO_2-based films the data is shown for both as-deposited samples and after annealing in Ar/H_2 gas at 600 °C. Also shown are the thermal conductivities for the purely inorganic thin films with thickness around 100 nm.

temperatures. For decreasing temperature the thermal conductivity values decrease – a fact that is often observed for superlattices and is ascribed to phonon population effects; Umklapp-type T^{-1}-dependence, typical for bulk materials is absent. This further supports the dominance of incoherent boundary-scattering.[75]

The thermal conductivity values for the oxide-organic superlattices described in this paper are in line with those reported by Liu *et al.* demonstrating ultra-low thermal conductivity in Zn-based hybrid thin films from DEZ and HQ or ethylene glygol precursors of the type, *m*:*k* = 1:1 or *m*=0, using the present notation.[31] Our recent results for the ZnO-based superlattices indicated that the phonon transmission through the molecular monolayers (from HQ) is actually hardly affected by the vibrational properties of the aromatic rings and that the suppression in thermal conductivity values is mainly due to the reduction in ZnO layer thickness, *i.e.*, the superlattice period.[75] This is consistent with the reduction in thermal conductivities for the TiO_2-based superlattices. Hence, in the future, it might be interesting to see if increasing the organic layer thickness (*k*>1) would enable exploitation of the vibrational-property difference between the organic and the oxide components and that way provide us with the means to further suppress the thermal conductivity in the present-kind inorganic-organic superlattices.

The thermal conductivity values can be notably suppressed for the inorganic-organic compositions for which the thermoelectric power factors remain essentially constant – a fact that raises high hopes for overall increase in *zT* values. It is of note, though, that the electronic properties have been reported in the in-plane direction and the thermal conductivity values in the cross-plane direction; it is evident that the next aim is to measure all these properties in the same direction.

So far, very few atomistic computational studies have been carried on thermoelectric inorganic-organic superlattice materials and as noted by Yang *et al.*, the fundamental understanding of phonon (and electron) transport across inorganic-organic molecular junctions remains at a very rudimentary level.[76] Carrete *et al.* investigated the thermoelectric properties of hybrid SiGe/thiophene superlattices using a combination of DFT and Green's function formalism.[77] They did not utilize explicit atomistic models of the actual inorganic/organic interfaces, as only the electronic and phonon properties of the constituent components were required in the applied formalism. They found out that due to the interplay between alloy scattering and phonon transmission at the molecular layers, very low thermal conductivities under 1 W m^{-1} K^{-1} and values of *zT* more than twice as large as those of bulk SiGe could be attained. Moreover, the alloyed nature of the inorganic SiGe turned out to be highly important: a superlattice whose inorganic part is made of pure silicon proved to be a poor choice for thermoelectric applications.

We have also carried out computational studies on the lattice thermal conductivity of the ZnO:HQ superlattices by combining DFT calculations with a full iterative solution of the Boltzmann Transport Equation for phonons (DFT-PBE/PAW level of theory).[34,78] Our first-principles lattice thermal conductivity calculations are in agreement with recent results for the ZnO:HQ superlattices, which indicate that the phonon transmission through the organic monolayers is actually hardly affected by the vibrational properties of the organic constituents and that the suppression in thermal conductivity values is mainly due to the reduction in ZnO layer thickness, that is, the superlattice period.[75] Figure 8 illustrates the cumulative lattice thermal conductivity of bulk ZnO (*T* = 300 K). To obtain the cumulative κ_l, only the heat-carrying phonons with a mean free path below a certain threshold are taken into account (*x*-axis of Figure 8). For ZnO:HQ superlattices, the cumulative κ_l can be used to estimate how the thermal conductivity of ZnO is reduced if the interfaces are considered to block all phonons having longer mean free paths than the ZnO block thickness. The experimentally observed thermal conductivities for the ZnO:HQ superlattices with ZnO:HQ ratios of 49:1 and 99:1 are 4.15±0.43 and 7.16±1.44 W m^{-1} K^{-1}, respectively.[33] The corresponding superlattice periods were estimated to be 8 and 16 nm, which allows comparisons with the predicted cumulative κ_l. Setting the maximum mean free path to 16 nm yields a cumulative κ_l of 5.0 W m^{-1} K^{-1}, which is in line with the experimental value measured for the 99:1 ZnO:HQ superlattice. The estimates coming out from this simple scheme are not expected to be quantitative. Decreasing the maximum mean free path further down to 8 nm yields a cumulative κ_l of 2.0 W m^{-1} K^{-1}, again somewhat underestimated, but reasonably in line with the experimental findings for the 49:1 ZnO:HQ superlattice. The quality of the κ_l estimates for ZnO:HQ superlattices that can be reached already by the simple inspection of the cumulative κ_l for bulk ZnO is encouraging considering computational high-throughput screening of potential novel inorganic-organic superlattices.

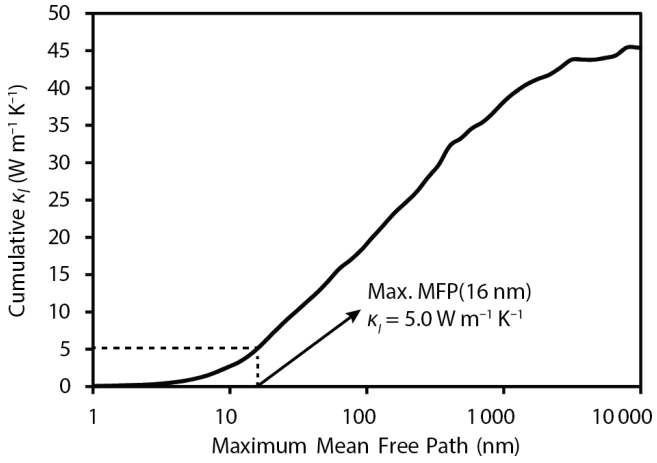

Figure 7. Cumulative lattice thermal conductivity of bulk ZnO (T = 300 K). The maximum mean free path of 16 nm would correspond to full phonon blocking organic layer in a 99:1 ZnO:HQ superlattice.

Summary and outlook

We have reviewed the structural and thermoelectric characteristics of hybrid inorganic–organic superlattice thin films that can be fabricated by combining the state-of-the-art ALD and MLD techniques in a highly controllable manner. The self-saturating film-growth mechanism inherent to these techniques allows for control of the hybrid inorganic-organic interface structures with the precision of a mono-molecular organic layer. Furthermore, it stems from the growth mechanism that the superlattice period – the key to control the thermoelectric properties – can be adjusted with equal precision. Highly promising proof-of-the-concept data have been gathered for the *n*-type (Zn,Al)O:HQ, (Ti,Nb)O_2:HQ and (Ti,Nb)O_2:C superlattices; systematic studies have shown that these hybrid materials retain the appealing thermoelectric characteristics of their purely inorganic matrixes, while the superlattice engineering enables significant reductions in their thermal conductivity.

Although the works so far carried out have been focused on oxide-organic materials there is no reason why the ALD/MLD fabrication method could not be extended more generally to inorganic-organic materials, as the library of the inorganic materials that can be fabricated with ALD is wide. Neither is the choice of the organic molecule limited to the reported ones but a large number of small molecules with variable functionalities is available; note also that the length of the polymers in the organic layers is freely tunable by adjusting the number of deposition cycles.

Of particular importance for the future thermoelectric devices based on inorganic-organic thin films would be to develop feasible ALD/MLD processes for *p*-type inorganic-organic thermoelectric superlattices. Such devices are anticipated to show not only enhanced thermoelectric characteristics but also attractive mechanical properties brought about by the organic constituents. This could enable the fabrication of thermoelectric devices on flexible and/or nanostructured substrates. We foresee that the ALD/MLD technique provides us with an elegant and versatile tool to realize such new materials and devices in a highly controlled and industrially feasible way.

Acknowledgements

The present work has received funding from the European Research Council under the European Union's Seventh Framework Programme (FP/2007–2013)/ERC Advanced Grant Agreement (no. 339478) and the Aalto Energy Efficiency Research Programme. A. J. K. gratefully acknowledges computing resources from the Finnish IT Center for Science (CSC) and funding from the Alfred Kordelin Foundation and the Foundation for Research of Natural Resources in Finland. Prof. Patrick Hopkins and his group (University of Virginia; TDTR measurements), and Dr. Tommi Tynell are acknowledged for collaboration and fruitful discussions.

References

1 G. J. Snyder, E. S. Toberer, *Nature Mater.*, 2008, **7**, 106-114.
2 R. Venkatasubramanian, E. Siivola, T. Colpitts, B. O'Quinn, *Nature*, 2001, **413**, 597-602.
3 M. S. Dresselhaus, G. Chen, M. Y. Tang, R. Yang, H. Lee, D. Wang, Z. Ren, J.-P. Fleurial, P. Gogna, *Adv. Mater.*, 2007, **19**, 1043-1053.
4 L. D. Hicks, T. C. Harman, X. Sun, M. S. Dresselhaus, *Phys. Rev. B*, 1996, **53**, R10493- R10496.
5 T. Koga, S. B., Cronin, M. S. Dresselhaus, J. L. Liu, K. L. Wang, *Appl. Phys. Lett.*, 2000, **77**, 1490-1492.
6 P. M. Norris, N. Q. Le, C. H. Baker, *J. Heat Transf.*, 2013, **135**, 061604-(1-13).
7 M. V. Simkin, G. D. Mahan, *Phys. Rev. Lett.*, 2000, **84(5)**, 927-930.
8 J. Ravichandran, A. K. Yadav, R. Cheaito, P. B. Rossen, A. Soukiassian, S. J. Suresha, J. C. Duda, B. M. Foley, C.-H. Lee, Y. Zhu, A. W. Lichtenberger, J. E. Moore, D. A. Muller, D. G. Schlom, P. E. Hopkins, A. Majumdar, R. Ramesh, M. A. Zurbuchen, M. A., *Nature Mater.*, 2014, **13,** 168-172.
9 W. S. Capinski, H. J. Maris, *Physica B*, 1996, **219&220**, 699-701.
10 T. Yao, *Appl. Phys. Lett.*, 1987, **51**, 1798-1800.
11 G. Chen, *J. Heat Transf.*, 1997, **119(2)**, 220-229.
12 P. Hyldgaard, G. D. Mahan, *Phys. Rev. B*, 1997, **56**, 10754.
13 G. Chen, *Phys. Rev. B*, 1998, **57(23)**, 14958-14973.
14 M. Kazan, P. Masri, *Surf. Sci. Rep.*, 2014, **69**, 1–37.
15 R. M. Costescu, D. G. Cahill, F. H. Fabreguette, Z. A. Sechrist, S. M. George, *Science*, 2004, **303**, 989-990.
16 C. Chiritescu, D. G. Cahill, N. Nguyen, D. Johnson, A. Bodapati, P. Keblinski, P. Zschack, *Science*, 2007, **315**, 351-353.
17 K. E. Goodson, *Science*, 2007, **315**, 342-343.
18 R. Y. Wang, R. A. Segalman, A. Majumdar, *Appl. Phys. Lett.*, 2006, **89**, 173113-(1-3).
19 P. J. O'Brien, S. Shenogin, J. Liu, P. K. Chow, D. Laurencin, P. H. Mutin, M. Yamaguchi, P. Keblinski, G. Ramanath, *Nature Mater.*, 2013, **12**, 118-122.
20 L. Hu, L. Zhang, M. Hu, J.-S. Wang, B. Li, P. Keblinski, *Phys. Rev. B*, 2010, **81**, 235427-(1-5).
21 W.-P. Hsieh, A. S. Lyons, E. Pop, P. Keblinski, G. D. Cahill, *Phys. Rev. B*, 2011, **84**, 184107-(1-5).
22 C. Wan, X. Gu, F. Dang, T. Itoh, Y. Wang, H. Sasaki, M. Kondo, K. Koga, K. Yabuki, G. J. Snyder, R. Yang, K. Koumoto, *Nature Mater.*, 2015, **14**, 622-627.
23 K.-H. Yoon, K.-S. Han, M.-M. Sun, *Nanoscale Res. Lett.*, 2012, **7**, 71-(1-6).
24 T. Tynell, I. Terasaki, H. Yamauchi, M. Karppinen, *J. Mater. Chem. A*, 2013, **1**, 13619-13624.

25 J.-P. Niemelä, M. Karppinen, *Dalton Trans.*, 2015, **44**, 591-597.
26 V. Miikkulainen, M. Leskelä, M. Ritala, R. L. Puurunen, *J. Appl. Phys.*, 2013, **113**, 021301-(1-101).
27 P. Sundberg, M. Karppinen, *Beilstein J. Nanotechnol.*, 2014, **5**, 1104-1136.
28 M. Knez, K. Nielsch, L. Niinistö, *Adv. Mater.*, 2007, **19**, 3425-3438.
29 J.-P. Niemelä, A. Giri, P. E. Hopkins, M. Karppinen, *J. Mater. Chem. A*, 2015, **3**, 11527-11532.
30 A. I. Abdulagatov, K. E. Terauds, J. J. Travis, A. S. Cavanagh, R. Raj, S. M. George, *J. Phys. Chem. C*, 2013, **117**, 17442-17450.
31 J. Liu, B. Yoon, E. Kuhlmann, M. Tian, J. Zhu, S. M. George, Y.-C. Lee, R. Yang, *Nano Lett.*, 2013, **13**, 5594-5599.
32 T. Tynell, A. Giri, J. Gaskins, P. E. Hopkins, P. Mele, K. Miyazaki, M. Karppinen, *J. Mater. Chem. A*, 2014, **2**, 12150-12152.
33 A. J. Karttunen, T. Tynell, M. Karppinen, *J. Phys. Chem. C*, 2015, in press., DOI: 10.1021/acs.jpcc.5b03433
34 A. J. Karttunen, T. Tynell, M. Karppinen, Thermoelectric Properties of Hybrid Inorganic–Organic ZnO:Hydroquinone Superlattices, 2015, manuscript.
35 T. Suntola, *Mater. Sci. Rep.*, 1989, **4**, 261-312.
36 S. M. George, *Chem. Rev.*, 2010, **110**, 111-131.
37 S. M. George, B. Yoon, A. A. Dameron, *Acc. Chem. Res.*, 2009, **42**, 498-508.
38 B. H. Lee, B. Y. Yoon, A. I. Abdulagatov, R. A. Hall, S. M. George, *Adv. Funct. Mater.*, 2013, **23,** 532-546.
39 Y. Du, S. M. George, *J. Phys. Chem. C*, 2007, **111**, 8509-8517.
40 M. Putkonen, J. Harjuoja, T. Sajavaara, L. Niinistö, *J. Mater. Chem.*, 2007, **17**, 664-669.
41 A. A. Dameron, D. Seghete, B. B. Burton, S. D. Davidson, A. S. Cavanagh, J. A. Bertrand, S. M. George, *Chem. Mater.*, 2008, **20**, 3315-3326.
42 Q. Peng, B. Gong, R. M. VanGundy, G. N. Parsons, *Chem. Mater.*, 2009, **21**, 820-830.
43 K. P. Klepper, O. Nilsen, H. Fjellvåg, *Dalton Trans.* 2010, **39**, 11628-11635.
44 K. P. Klepper, O. Nilsen, P.-A. Hansen, H. Fjellvåg, *Dalton Trans.* 2011, **40**, 4636-4646.
45 A. Sood, P. Sundberg, M. Karppinen, *Appl. Surf. Sci.*, 2011, **257**, 6435-6439.
46 P. Sundberg, A. Sood, X. Liu, L.-S. Johansson, M. Karppinen, *Dalton Trans.* 2012, **41**, 10731-10739.
47 B. H. Lee, B. Yoon, V. R. Anderson, S. M. George, *J. Phys. Chem. C*, 2012, **116**, 3250-3257.
48 P. Sundberg, A. Sood, X. Liu, L.-S. Johansson, M. Karppinen, *Dalton Trans.*, 2013, **42**, 15043-15052.
49 T. Tynell, H. Yamauchi, M. Karppinen, *J. Vac. Sci. Technol. A*, 2014, **32**, 01A105-(1-5).
50 J. Malm, E. Sahramo, J. Perälä, T. Sajavaara, M. Karppinen, *Thin Solid Films*, 2011, **519**, 5319-5322.
51 T. Tynell, M. Karppinen, *Semicond. Sci. Technol.*, 2014, **29**, 043001-(1-15).
52 A. C. Ferrari, J. Robertson, *Phys. Rev. B*, 2000, **61(20)**, 14095-14107.
53 E. A. Carter, *Science*, 2008, **321**, 800-803.
54 S. Curtarolo, G. L. W. Hart, M. B. Nardelli, N. Mingo, S. Sanvito, O. Levy, *Nature Mater.*, 2013, **12**, 191-201.
55 R. Dovesi, B. Civalleri, R. Orlando, C. Roetti, V. R. Saunders, Ab Initio Quantum Simulation in Solid State Chemistry, in Reviews in Computational Chemistry, K. B. Lipkowitz *et al.* (ed.), **Vol 21**., 2005, Wiley-VCH.
56 C. Draxl, D. Nabok, K. Hannewald, *Acc. Chem. Res.*, 2014, **47**, 3225–3232.
57 K. Noori, F. Giustino, *Adv. Funct. Mater.*, 2012, **22**, 5089–5095.
58 Y. Xu, O. T. Hofmann, R. Schlesinger, S. Winkler, J. Frisch, J. Niederhausen, A. Vollmer, S. Blumstengel, F. Henneberger, N. Koch, P. Rinke, M. Scheffler, *Phys. Rev. Lett.*, 2013, **111**, 226802-(1-5).
59 O. T. Hofmann, J.-C. Deinert, Y. Xu, P. Rinke, J. Stähler, M. Wolf, M. Scheffler, *J. Chem. Phys.*, 2013, **139**, 174701-(1-10).
60 T. Tynell, M. Karppinen, *Thin Solid Films*, 2014, **551**, 23-26.
61 P. Banerjee, W.-J. Lee, K.-R. Bae, S. B. Lee, G. W. Rubloff, *J. Appl. Phys.*, 2010, **108**, 043504-(1-7).
62 T. Tynell, H. Yamauchi, M. Karppinen, *J. Vac. Sci. Technol. A*, 2013, **31**, 01A109-(1-4).
63 Y. Furubayashi, T. Hitosugi, Y. Yamamoto, K. Inaba, G. Kinoda, Y. Hirose, T. Shimada, T. Hasegawa, *Appl. Phys. Lett.*, 2005, **86**, 252101-(1-3).
64 H. Nogawa, T. Hitosugi, A. Chikamatsu, S. Nakao, Y. Hirose, T. Shimada, H. Kumigashira, M. Oshima, T. Hasegawa, *Jpn. J. Appl. Phys.*, 2010, **49**, 041102-(1-4).
65 Y. Hirose, N. Yamada, S. Nakao, T. Hitosugi, T. Shimada, T. Hasegawa, *Phys. Rev. B*, 2009, **79**, 165108-(1-5).
66 J. Jaćimović, R. Gaál, A. Magrez, J. Piatek, L. Forró, S. Nakao, Y. Hirose, T. Hasegava, *Appl. Phys. Lett.*, 2013, **102**, 013901-(1-3).
67 C. Tasaki, N. Oka, T. Yagi, N. Taketoshi, T. Baba, T. Kamiyama, S.-I. Nakamura, and Y. Shigesato, *Jpn. J. Appl. Phys.*, 2012, Part **51**, 035802-(1-5).
68 J. Aarik, A. Aidla, T. Uustare, V. Sammelselg, *J. Cryst. Growth*, 1995, **148**, 268-275.
69 V. Pore, M. Ritala, M. Leskelä, T. Saukkonen, M. Järn, *Cryst. Growth Des.*, 2009, **9**, 2974-2978.
70 J.-P. Niemelä, H. Yamauchi, M. Karppinen, *Thin Solid Films*, 2014, **551**, 19-22.
71 J.-P. Niemelä, Y. Hirose, T. Hasegawa, M. Karppinen, *Appl. Phys. Lett.*, 2015, **106**, 042101-(1-4).
72 D. G. Cahill, *Rev. Sci. Instrum.*, 2004, **75(12)**, 5119–5122.
73 A. J. Schmidt, X. Chen, G. Chen, *Rev. Sci. Instrum.*, 2008, **79**, 114902-(1-9).
74 P. E. Hopkins, J. R. Serrano, L. M. Phinney, S. P. Kearney, T. W. Grasser, C. T. Harris, *J. Heat Transfer*, 2010, **132**, 081302-(1-10).
75 A. Giri, T. Tynell, J.-P. Niemelä, J. Gaskins, B. F. Donovan, M. Karppinen, P. E. Hopkins, Phonon scattering and heat transport mechanisms in atomic/molecular layer-deposited hybrid organic/inorganic superlattices, 2015, Manuscript.
76 J. Yang, H.-L. Yip, A. K.-Y. Jen, *Adv. Energy. Mat.*, 2013, **3**, 549-565.
77 J. Carrete, N. Mingo, G. Tian, H. Ågren, A. Baev, P. N. Prasad, *J. Phys. Chem. C*, 2012, **116**, 10881–10886.
78 W. Li, J. Carrete, N. A. Katcho, N. Mingo, *Comput. Phys. Commun.*, 2014, **185**, 1747-1758.

TOC

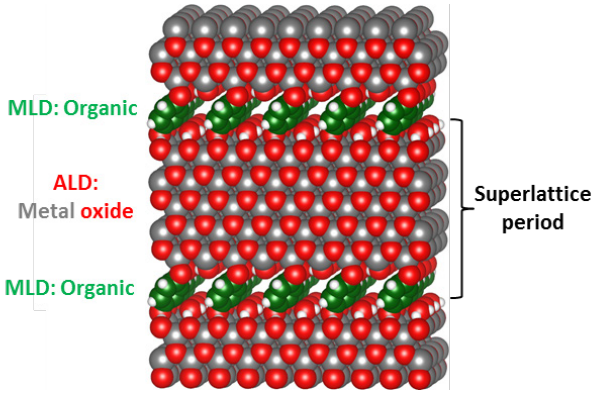
MLD: Organic
ALD:
Metal oxide
MLD: Organic
Superlattice
period